Intelligent Framework for Mineral Segmentation and Fluid-accessible Surface Area

- 2 Analysis in Scanning Electron Microscopy
- 3 Parisa Asadi¹, Lauren E. Beckingham^{1*}
- ¹Civil and Environmental Engineering, Auburn University, Auburn, AL, United States
- 5 *Corresponding author: leb@auburn.edu

6 HIGHLIGHT

- Random Forest and U-Net models used to identify minerals in SEM BSE and EDS images.
- Predicted porosity, mineral abundance and accessibility comparable to ground-truth data.
- Filter-based U-Net and Random Forest models had a comparable performance to the BSE-EDS
 based models.
- Image grayscale variation makes machine learning models rely more on extracted features and mineral patterns.
- Dissolution risk assessment map proposed to identify locations most susceptible for reaction.

14 Keyword

17

1

- 15 Reactive surface area analysis, Mineral volume fraction and accessibility, Machine learning, SEM
- imaging, Dissolution risk assessment map, U-Net, Random Forest.

18 ABSTRACT

Imaging is powerful means of sample characterization where mineral abundances and surface areas can be quantified from mineral maps. Images are typically manually processed by domain experts, which is time-consuming, labor intensive, and subjective. Emerging techniques, such as machine learning based image processing, can potentially address these limitations and accelerate image processing but the performance of these models for accurate sample characterization and surface area analysis has not been completely evaluated. This study evaluates the potential of Random Forest and U-Net machine learning methods for mineral characterization and surface area analysis of six sandstone samples. Various input variable sets including filter extracted features, scanning electron microscopy (SEM) backscatter electron (BSE) images and SEM-energy dispersive x-ray spectroscopy images (EDS) images were considered. The evaluation was conducted by providing an intelligent framework that not only evaluates the accuracy of prediction for each pixel but also investigates the accuracy of predicted neighboring pixels. In addition, a new methodology is proposed to distinguish the more susceptible places to dissolution on the surface of a given mineral using a ranked mineral dissolution risk assessment map. The results showed both methods had an acceptable performance with the U-Net model outperforming Random Forest. Both methods showed an improved accuracy when filter extracted features were added to the dataset as input variables. The models' performance predicting mineral abundances and accessibility agreed well with ground truth data for majority classes (e.g., quartz) compared to minority classes. Finally, the proposed methodology was shown to reliably identify the locations susceptible for dissolution indicated via proposed risk assessment maps. The intelligent segmentation and surface area analysis framework is a promising tool for accelerating the processing of SEM data and reactivity assessment of samples.

1. Introduction

24

25

26

27

28

29

30

31

32

33

34

35

36

37

38

39

40

41

42

43

44

45

46

Micro-porosity imaging is a valuable technique for characterizing mineral/pore spatial distributions in the fields of geosciences and environmental engineering. The extracted parameters such as porosity, mineral abundance, texture, fracture distribution, and accessible mineral surface areas (*Qin and Beckingham 2019; Landrot et al. 2012; Peters 2009; Ma et al., 2021; Luhmann et all., 2017*) are the basis for digital rock analysis (*Asadi and Beckingham, 2021; Kim et al., 2021;*

47 Brunhoeber et al., 2021; Anovitz et al., 2022) and other related computational simulation works. 48 Reactive transport models utilize this information to simulate geochemical reactions that vary from 49 a chemical weathering induced mineral dissolution (Chen et al., 2020a; Mahdikhani et al., 2018; 50 Deng et al., 2020), to rather complex CO₂-brine-mineral interactions in carbon capture and storage 51 (CCS) systems (Beckingham et al., 2017; Qin and Beckingham, 2019) and reactions in multimineral subsurface energy storage (Koohi-Fayegh and Rosen, 2020; Iloejesi and Beckingham 52 2021a&b) and enhanced oil recovery (Esene et al., 2019; Sevyedi et al., 2018) Systems. 53

54 Scanning electron microscopy backscattered electron microscopy (SEM-BSE) imaging is a 55 powerful technique for mineral analysis and microstructure characterization (Li et al., 2021; 56 Peters, 2009). SEM imaging incorporating energy-dispersive X-Ray spectroscopy (EDS) 57 elemental maps enable classification of minerals and facilitates quantification of mineral phases, including those with abundance less than the X-ray diffraction (XRD) detection limit (Landrot et al. 2012). Although XRD is a great source for mineral identification, it cannot provide any spatial information. In addition, XRD has noted limitations for distinguishing the minority mineral phases based on the instrument used, often 1% (Landrot et al., 2012) to 5% (Beckingham et al., 2017) 62 Salek Et al., 2022). These types of limitations do not restrict identification of minority phases via SEM-BSE and EDS imaging.

58

59

60

61

63

64

65

66

67

68

69

70

71

Extracted data from SEM-BSE and EDS imaging is useful for assessing sample properties or parameterize reactive transport simulations to consider reactivity under a specified set of conditions (Beckingham et al. 2017). Quantification of mineral volume fractions and accessible surface areas are of particular interest where accessible surface area refers to mineral surfaces in contact with reactive fluids. Beckingham et al. (2017) found that simulations carried out using mineral accessible surface areas quantified from mineral/pore segmented images better reflected the reaction rates observed in core-flood experiments than simulations that used the specific surface areas measured via BET.

Despite advances in image processing and analysis, segmenting of SEM-BSE and EDS images is challenging. Images either need to be processed by software with a large element composition-to-mineral database such as Quantitative Evaluation of Minerals by Scanning Electron Microscopy (QEMSCAN) (*Pirrie et al., 2004*) or to be conducted by experienced expert technicians (*Asadi and Beckingham, 2021; Brunhoeber et al., 2021; Kim et al., 2021*), both of which are expensive, time-consuming, labor-intensive, and subjective. Machine learning (ML) based methods have emerged as a relatively new and open-source approach for mineral classification.

Machine learning for geoscience and environmental engineering applications has included mineral characterization (*Karimpouli and Tahmasebi, 2019; Li et al., 2021; Chen et al., 2020b*), spatial distribution mapping (*Kim et al., 2021*), rock typing and permeability prediction (*Mohammadian et al., 2022, Yoon and Melander, 2021*). Pore-scale imaging has advanced crucially through the integration of machine learning with imaging techniques (*Asadi and Beckingham, 2021; Kim et al., 2021*). While prior work has considered use of machine learning for mineral segmentation in SEM images (*Li et al., 2021*), the performance of machine learning models for mineral characterization of SEM images based on mineral abundance and accessible surface area analysis, which is the focus of this work, has not been considered.

Using mathematical models, machine learning excavates nonlinear underlying patterns in a dataset (*Chen et al., 2020b; Zhang et al., 2022, Asadi and Beckingham 2021; Suthaharan, 2016*). Models can simultaneously consider several extracted features in addition to the color or grayscale intensity for a more reliable mineral/pore segmentation. This ability is valuable for segmenting individual minerals with similar or overlapping grayscale intensity in SEM BSE images as well as addressing grayscale color variations from one sample to the other due to different device

parameter setups such as brightness or contrast. In these cases, extracted features of minerals are key to successful mineral/pore segmentation (*Asadi and Beckingham 2021; Suthaharan, 2016*). Relying only on gray-scale intensity for training of machine learning models can lead to unstable models with less generalization to other datasets due to intensity variation among different images and intensity overlaps of different minerals. Combining image datasets with image filtering techniques as inputs to machine learning models can potentially improve mineral quantification and surface area analysis from images. This is because filters can find underlying patterns in minerals and therefore improve the prediction results.

This study aims to provide an intelligent platform for auto-segmentation of mineral/pore phases in SEM images, using mineral volume fractions and accessible surface area to evaluate performance. Two widely used machine learning methods, Random Forest and U-Net are used to process images of sandstone samples and mineral volume fractions and accessible surface areas determined from machine learning-processed images and compared with data from manually-processed images. A quantitative dissolution risk assessment analysis that identifies locations more susceptible to dissolution by taking the predicted results for neighboring pixels into account is proposed. The prepared framework will help geologists obtain the mineralogy, mineral/pore spatial distribution, and the mineral reactivity risk assessment maps for sandstone samples reliably and quickly based on SEM images. This automated and open-source framework to estimate mineral abundance and accessibility is also desirable to reduce time and resource requirements to obtain sample characteristics and inform reactive transport simulation models.

2. Data and Methodology

2.1 Sandstone Samples

Processed mineral maps for six sandstone samples introduced in our previous work (*Salek et al. 2022*) were selected for machine learning model training and analysis. Data included processed maps of Bandera Brown, Bentheimer, and Kentucky sandstones (samples purchased from Kocurek Industries), Lower Tuscaloosa and Paluxy sandstones (samples from Geological Survey of Alabama), and an additional Paluxy sandstone from Kemper County pilot CO₂ injection site (*Qin and Beckingham, 2019*). In addition, a new pooled dataset was created and considered by the models which was the combination of the images of the six sandstone samples (referred to as the pooled dataset). The XRD data (Table1) and prior compositional analyses of the samples showed that they are mainly quartz (66% - 94%), with various amounts of feldspars, carbonate and clay minerals, and trace amount of other mineral species such as chlorite, with porosity ranging from 0.14 to 0.33 (Kocurek Industries; Guan 2012; Soong et al. 2016; Salek et al., 2022; Qin and Beckingham, 2019).

Table 1. XRD composition analysis of the samples obtained from Kocurek Industries ¹, Guan² (2012) and Soong et al.³ (2016).

Sandstones	XRD Source	Porosity	Quartz	Albite	Microcline	Calcite	Dolomite	Kaolinite	Illite	Chlorite
Bandera Brown ¹	SPE-178999	22-23	66	13	2	3	0	3	11	2
Bentheimer ¹	SPE-174666	24	94.4	1.2	1.2	0.5	0			
Bandera Gray ¹	SPE-173736	20-21	59	12	0	0	15	3	10	1
Kentucky ¹	SPE-147395	14	66	17	3	0	0	trace	14	0
Paluxy ²		20-25	69.3	24.5	1.2	0.8		2.3	0.2	
Lower Tuscaloosa ³		30-33	92	0.5	1.6		1.5	3.7		

2.2 SEM BSE-EDS and Labeled Images

SEM BSE images of the samples used in this work and their corresponding EDS elemental maps were captured using a ZEISS EVO 50VP Scanning Electron Microscope at Auburn University and

analyzed in our previous work (*Salek et al.*, 2022; Qin and Beckingham 2019). SEM images were captured at resolutions ranging from 0.34 μm to 5.71 μm. Eight SEM-EDS elemental maps were used in this study including aluminum (Al), magnesium (Mg), sodium (Na), potassium (K), calcium (Ca), silicon, (Si), iron (Fe), titanium (Ti). Image acquisition was performed on single image field of views for all samples except for the Paluxy sandstone from Kemper County pilot CO2 injection site (Qin and Beckingham, 2019) that was generated from multiple image fields and was tiled to create a main image with the resolution of interest (0.34 μm). Mineral phases were identified based on relative grayscale intensity and elemental signatures (Peters, 2009), with knowledge of anticipated minerals from XRD data (Salek et al. 2022; Qin and Beckingham, 2019). The detailed information about the SEM-BSE and EDS image acquisition and device set up are provided in Qin and Beckingham (2019) and Salek et al. (2022), and detailed image processing methodology and its cross validation with XRD data can be found in Landrot et al. (2012) and Beckingham et al. (2017).

Here, to train the models and validate the machine learning models' performances, mineral maps were labeled with a specific label value assigned to each mineral as the ground truth value. Figure 1 shows an example of labeled image and its corresponding colors. As evident in the Figure, the samples were mainly comprised of quartz, carbonates, K-feldspar and albite. Table 2 shows the number of pixels of each mineral class for the six samples that 70%, 15% and 15% were used for training, validation, and test, respectively.

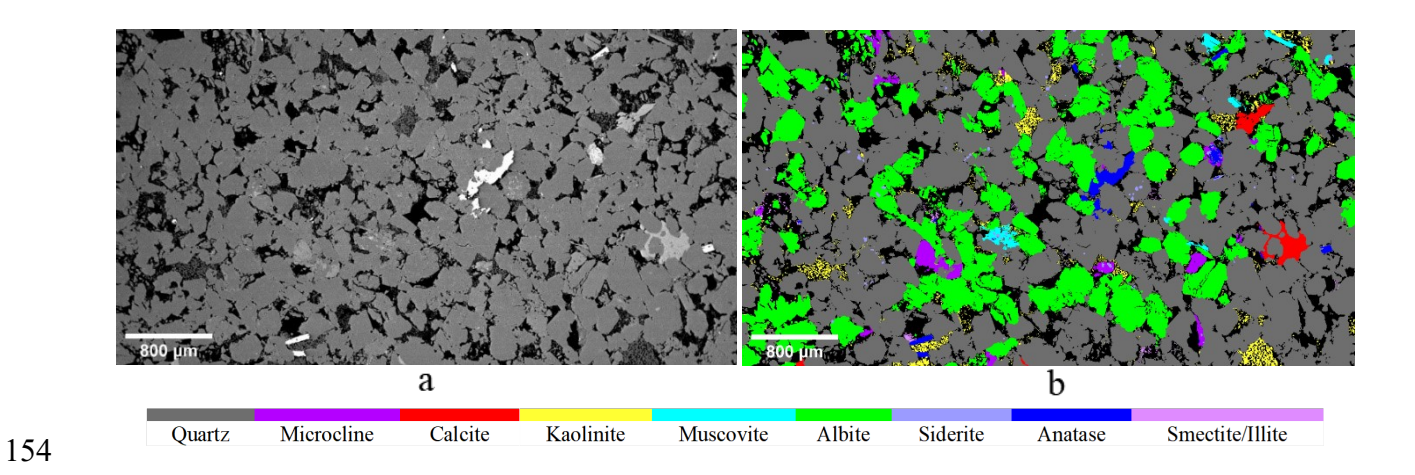


Figure 1. a) 2D SEM BSE image of a thin section from the Paluxy formation with image resolution of 1.9 μm, and image size of 17.14 mm² (reproduced from *Salek et al., 2022*), b.) Mineral phase segmented image.

Table 2. Labeled mineral/pore pixels for the samples.

Mineral	Label	Bandra Brown	Lower Tuscaloosa	Bentheimer	Kentucky	Bandera Gray	Paluxy Sample1	Paluxy Sample2
Pore	"0"	443623	144457	1616132	1145212	2552360	2673382	8183063
Quartz	"1"	1144567	267011	2845788	279728	727147	891332	19279109
Albite	"2"	159540	1396	74450	307767	411706	944590	
Kaolinite	"3"	67063	10623				87317	
Smectite/I llite	"4"	18267			215434	256845	9163	1791284
K- Feldspar	"5"	129752	4577	81431	53458	487745	46501	1058115
Chlorite	"6"	7581						
Magnetite	"7"	23169			47663			
Anatase	"8"	7333			3042	11581	31302	
Carbonate	"9"	105	4321	75		228996	30133	2615561
Muscovite	"10"		1510		46492	27582	23082	105808
Zircon	"11"				6672			
Ilmenite	"12"			10284	5362			
Siderite	"13"						11079	528404
Biotite	"14"					45734		

2.3 Feature Extraction

Minerals have different visible characteristics like texture and grain size which make them distinguishable from one another. Filtering techniques convolute the original images such that

additional features may be reliably extracted for machine learning models to differentiate minerals with similar color intensity (*Asadi and Beckingham, 2021*). In this study, well-known filters, including difference of Gaussian, Median, Non-local mean, Bilateral, vertical and horizontal Sobel filters, were applied to the sandstone BSE images using the OpenCV (*Bradski and Kaehler, 2008*) and Scikit-image (*Van der Walt et al., 2014*) libraries of Python. These filters provide feature maps representative of texture, grain size, edges and color variation. For instance, the Sobel and Bilateral filters are used to extract edge features and textures, while difference of Gaussians is utilized for blobs and corners (*Asadi and Beckingham 2021*).

2.4 Establishing the Datasets

In this study, BSE images, elemental EDS maps, and extracted features were used as input variables for machine learning models. Labeled images were established as ground truth images for each sample and introduced to the models to be trained for mineral/pore segmentation. In addition to these individual sample datasets, a pooled dataset which was a combination of all samples was generated to further investigate feature-based machine learning mineral/pore segmentation on a more general and comprehensive database. For the Random Forest model, the input was the pixel-level grayscale values extracted from the BSE image, elemental maps (including Al, Mg, Na, K, Ca, Si, Fe, Ti), and filter extracted features (including difference of Gaussian disk 1 and 10, Bilateral, Median-blur, non-local Means, and Sobel filter in x and y directions). The label data was the mineral class that ranged from 0 to 14 for each pixel. The U-Net model was trained end-to-end where the input was images cut from the stacked BSE image, the elemental maps (i.e., Al, Mg, Na, K, Ca, Si, Fe, Ti), and the filter extracted features (i.e., difference of Gaussian disk 1 and 10, Bilateral, Median-blur, non-local Means, and Sobel filter in x and y directions), while the output was the corresponding mineral labels.

2.4.1 Dataset for Random Forest

The Random Forest training dataset for each sample had a shape of m×n, where m was the number of pixels, and m was the number of input variables obtained from the eight elemental EDS maps, BSE intensity image, and the six filter extracted feature maps (Table 2). The BSE and EDS intensity values at each pixel were extracted from the grayscale maps. Intensity values range from 0 (black) to 255 (white) and brighter pixels reflect higher elemental intensities in EDS maps and bigger average atomic numbers in BSE images. The brightness/intensity values of filter extracted features demonstrates various patterns such as entropy or edges in the associated BSE images.

To create the database, each input variable was first normalized to transform data to the range of 0–1 by dividing each pixel value by the maximum value for that specific input variable. The input variable values at the same pixel location were then extracted as a vector containing 15 input values, including the inputs from BSE, EDS, and filter extracted features. The mineral/pore class labels at the corresponding output pixels were the ground truth data with 15 mineral/pore classes (Table 2). The dataset for the samples was imbalanced as they were mainly comprised of quartz, feldspars, and calcite. To address this issue, different weights were assigned to each class that was proportional to the inverse percent size of each class within the dataset. Thus, a matrix with the size of the number of pixels in each dataset × 15 was used as input, where 15 denotes the number of input variables extracted at each data point.

The ground truth data was a vector with the size of the number of pixels in each dataset × 1 which contained the value of the mineral/pore class labels. The dataset of each sample was randomly split into training (70%), validation (15%) and test (15%) datasets to train and evaluate the Random Forest model.

2.4.2 Dataset for U-Net

Unlike the Random Forest model with pixel-level classification, where the input data was a matrix of shape m×n, the training process for the U-Net model was end-to-end and utilized neighboring pixels, which allows for segmented regions with less noise. To create the dataset, the stacked and normalized input images were cropped into smaller training samples (128×128 pixels). Then, using a data augmentation procedure that including flipping in both vertical and horizontal directions, zooming, shifting, and rotation, the amount of data was increased to have more data for improved prediction. For the pooled dataset, each input sample had a total of 15 channels (input variable set), while the output had 15 channels for each mineral/pore class. After data augmentation, there were a total of 8,505 samples (Table 2) for training and testing, which were further divided into training, validation, and testing, with the fractions of 70%, 15% and 15%.

2.5 Pixel Wise Image Analysis and Segmentation Algorithms

2.5.1 Random Forest Machine Learning Model

Random Forest (*Breiman 2001*) is one of the powerful ensemble learning methods that combines m random decision trees (mtree) trained on different subsamples of data into a decision forest ($Asadi \ and \ Tian, \ 2021$) to solve regression/classification problems. The grown forest algorithm not only has higher precision over individual decision trees such as CART, but also is relatively unbiased to multivariate common linearity and imbalanced data ($Asadi \ and \ Beckingham \ 2021$; $Asadi \ and \ Tain \ 2021$) which makes it appealing for phase segmentation.

For training, the model randomly selects N subsamples from the training dataset using a Bootstrapping technique. Each sample set is used to construct a decision classification tree, each of which randomly selects k input variables and starts with a single node. Each node in the decision tree is a weak binary classifier which selects the various parameters (e.g., k input variables or a

variable attribute) to maximize the classification index, whereas the final leaf node includes a discriminator to assign each pixel to a specific class. In Random Forest, each tree finds new splits and builds out it's nodes while minimizing the Gini impurity (equation 1) for each split based on its information and patterns in a subsample of the training set, eventually stopping at leaf nodes when it reaches the maximum depth of tree or the minimum number of samples per node.

In general, each node in a forest seeks to minimize the impurity index. In this study, the Gini index that is one of the most common impurity functions was used. The function is given by,

237 Gini (p) =
$$\sum_{k=1}^{k} p_k (1 - p_k) = 1 - \sum_{k=1}^{k} p_k^2$$
 (1)

where p_k is probability that the sample belongs to class k. This represents the likelihood of misclassification of a random data point at a certain node if the data point were classified randomly. When the Gini coefficient is the smallest, the purity is the highest and the uncertainty is the smallest.

In this study, the Scikit-Learn library of Python was used to implement the Random Forest model (*Pedregosa et al., 2011*). At first, a model with 200 random trees (i.e., ntree = 200), each with unlimited depth and no pruning, was created. Randomly selected k input variables (estimated as the square root of the numbers of predictors, i.e., $ktry \approx 4$) from all input variables were selected at each node to train the model. Next, the model's hyperparameters were fine-tuned. For ktry and ntree tuning, the random search was incorporated by grid searching the ntree in the range of 30 to 700 and ktry in the rage of 2 to 8, resulting in the final forest of ntree = 50 and ktry = 4. The depth of tree changed from 15 to 4×15 and the best one was 32. The minimum sample per split was selected to be five based on random number search in the range of three to ten.

2.5.2 Modified U-Net Deep Learning Model

251

252

253

254

255

256

257

258

259

260

261

262

263

264

265

266

267

268

269

270

271

272

The U-Net method (Ronneberger et al., 2015), a fully connected Convolutional Neural Network (CNN) method, was originally proposed to efficiently capture nuances required in the analysis of medical images. Ever since, it has become a standard tool for various classification problems and shown great performance by using less images and outputting more precise segmentation maps (Asadi and Beckingham, 2021; Kim et al., 2021). The architecture is based on a symmetric encoder-decoder approach which resembles a U-shaped structure. The encoder consists of contraction blocks to capture context via feature extraction. Each block takes a 128 by 128 input image to apply two convolutional kernels of 3 by 3, followed by a rectified linear transformation and a max-pooling operation with a stride of 2 by 2. The max-pooling process reduces spatial information while convolutional kernels increase feature channels in the the encoder path allowing the network to learn complex structures effectively due to propagating context information to higher dimensions (Asadi and Beckingham, 2021). The decoder is responsible for precisely retrieving spatial information along the up sampling, where the output of each convolutional level is combined with high resolution features from the contraction part through skip connection ports. The expansion blocks in the decoder pass the input to two convolutional layers followed by a 2 by 2 up-sampling layer. In the decoder, while the image size gradually increases, the feature depth gradually decreases. At the end of the network, the feature images were passed through a 1 by 1 convolutional layer with a SoftMax activation function to perform the multi-layer semantic segmentation and provide the probability of each pixel, and map M features which are desired minerals/pore classes. The class associated with the highest estimated probability would then be the one assigned to that pixel.

This classification scheme was implemented in Python using the TensorFlow and Keras packages. Here, stacked BSE, EDS and filter extracted features from the original BSE images as well as their corresponding segmented maps were used for training. Several loss functions including focal (equation 2) and categorical cross-entropy were utilized and applied to adjusted weights and biases for finding the best performing one. The focal loss function, which is designed to counteract class imbalance, had the best performance and is used in this study. In the focal loss function, each class is down-weighted such that their contribution to the total loss is small even if their number is large. The function is given by,

Focal Loss
$$(p_t) = -\alpha_t (1 - p_t)^{\gamma} log(p_t)$$
 (2)

where p_t is the probability of a given class, α is a regulator parameter range from [0, 1], and γ controls the penalizing power of the model to the error and is an integer number greater than zero (γ >0). When γ = 1, the focal loss function works like the cross-entropy loss function. In this study, γ = 2 and α = 1 were set due to better performance. Adaptive moment estimation (ADAM) was selected as the optimizer to iteratively adapt the network's learning rate and early-stopping was used to prevent overfitting. Fine-tuning function of the TensorFlow library was used for the number of epochs varied from 100 to 1000 (epoch = 300 was the best one) and the learning rate (LR) from 10^{-6} to 10^{0} (LR = 0.0001 was the best one). Note that normalized datasets, with an interval of [0, 1], were used here so that the models could converge faster.

2.6 Mineral/pore Quantification and Surface Area Analysis

In this study, the performance of machine learning models for mineral/pore quantification and surface area analysis was evaluated. The porosity, mineral abundance, and mineral accessibility values were determined in predicted mineral maps and cross compared to the grand-truth data quantified from 2D labeled BSE-EDS images. The porosity values and volume fraction of mineral

phases (mineral abundance) were determined by counting pore pixels and mineral pixels with the same color, respectively. The percentage of each mineral's surface that is adjacent to the pores (mineral accessibility) then were quantified by counting mineral pixels adjacent to pore pixels. Here, accessibility is based on the assumption that all pores are connected or would be accessible to reactive fluids.

2.6.1 Ranked Mineral Dissolution Risk Assessment

Here, a new concept, a ranked mineral dissolution risk assessment map, that inherits the name and application from groundwater vulnerability and risk assessment maps but for mineral dissolution assessment, is introduced. The ranked mineral dissolution risk assessment map is used here as a means of evaluating the model predicted maps and checking their goodness of fit for extracting reactive sample characteristics not only pixel wise but also considering adjacent neighbors.

To create the ranked mineral dissolution risk assessment map, we first assigned a rank number to each pixel, ranging from 1 for less reactive minerals (i.e., quartz) to 14 for highly reactive ones (i.e., calcite, dolomite) for a specific set of conditions. Pores were assigned the highest (15) assigned rank number. The mineral rankings were based on dissolution rates obtained from Brantley (2008), Yadav and Chakrapani (2006), and Zhang et al. (2015) at pH 5 and a temperature of 298 K. Next, the pixel-wise risk number for each individual mineral was determined based on the highest adjacent ranked pixel to the pixel of interest.

The ranked mineral dissolution risk assessment map will help further assess the spatial distribution of reactivity risk for a given mineral and its evolution of risk. This map only considers the potential risk of being exposed to fluid to provide a conceptual reactive risk assessment map. The higher assigned rank, the higher the risk for the given pixel to be exposed to the fluid and to

be involved in a rection over time compared to other pixels with similar mineralogy but less dissolvable adjacent neighbors.

2.7 Performance Metrics

To evaluate the performance of machine learning-based models, accuracy, precision, recall, and F1-score performance metrics were used. Precision calculates how often the model's prediction is correct over all positive predictions of a given class, whereas recall or sensitivity measures how accurate the model is in detecting true positive classes (relevant data). F1-score is the tradeoff between recall and precision and takes both *TP*, data points truly predicted as the class under consideration, and *FN*, incorrect rejection of that class, into account. They are defined as:

326 F1 =
$$(2 \times \text{precision} \times \text{recall})/(\text{precision} + \text{recall})$$
 (3)

$$327 \quad \text{precision} = \text{TP/(TP + FP)} \tag{4}$$

$$328 \quad \text{recall} = \text{TP/(TP} + \text{FN)} \tag{5}$$

The test image set was compared against the ground truth images to evaluate the models. To calculate the binary F1-score for each class, the given class was considered individually as positive, with the other classes as negative. Once the score was calculated for every class, their mean values were computed to evaluate the macro performance of the classifiers. However, this analysis does not consider a potential class imbalance among the samples as it weighs all classes equally. Thus, for a fairer global performance evaluation, we also estimated the overall statistics by computing the weighted average of each evaluation metric with respect to the representativity of each class.

3. Results and Discussion

3.1 Performance of the models on single and pooled datasets

This section investigates the effect of different image datasets with various grayscale distribution on the U-Net and Random Forest classifier's performances. Samples (i.e., individual sandstone samples as well as the pooled dataset) had different image resolution, size, range of gray scale intensity, and several mineral components. Figure 2 presents the loss and accuracy of the trained U-Net model as a function of epoch for the pooled dataset. As shown, the loss in the pooled dataset decreases significantly after five epochs, while the accuracy of the U-Net model improves to around 96% after a few epochs. Similarly, the Random Forest classifier for the pooled dataset reaches an accuracy of 92%. A similar trend is obtained for individual datasets with accuracy ranging from 85% to 95%. The loss and accuracy plots for individual samples as well as for the pooled dataset for the Random Forest model are provided in the supplementary materials (Figs. S1 – S3).

By comparing the results of individual samples results (Figs. S1 - S3) with the pooled dataset (Figure 2), it can be concluded that using a larger dataset (i.e., pooled dataset) can improve the results. In general, the U-Net model trained on the pooled dataset reaches a lower loss value with fewer epochs, obtaining a higher accuracy and outperforming the individual datasets. The same is evident for the Random Forest model where the model trained on the pooled dataset achieves a better score compared to individual sets.

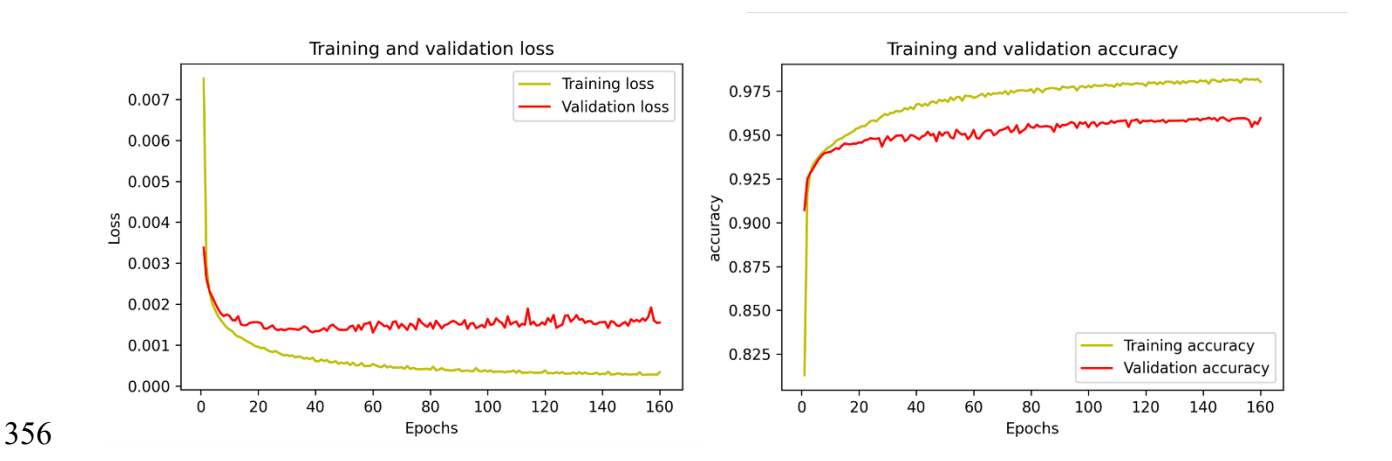


Figure 2. The accuracy and loss against the number of epochs for the U-Net model trained on pooled dataset.

3.2 Effect of input variable on the models' performance

The pooling of different sandstone samples together provides a dataset with varied grayscale intensity values but similar mineral characteristics such as mineral size, texture, patterns, etc. Therefore, to make a better prediction, machine learning algorithms must rely on the underlying patterns in addition to the BSE grayscale values. This section presents the models' performances on predicting mineral/pore classes with different input variable sets (i.e., BSE gray intensity, elemental EDS maps, and filter extracted features).

Figure 3 shows the F1-score of pores and mineral classes calculated for the predicted results of U-Net and Random Forest models on the pooled dataset. Different colors reflect different input variable sets, where the results of the Random Forest and U-Net classifiers trained with only the gray-scale BSE image (blue in Fig. 3) have 56% and 88% accuracy, respectively. As shown, the BSE-based model cannot predict minority classes such as zircon, chlorite, siderite and biotite and has a fair performance identifying albite due to its similar grayscale intensity as quartz.

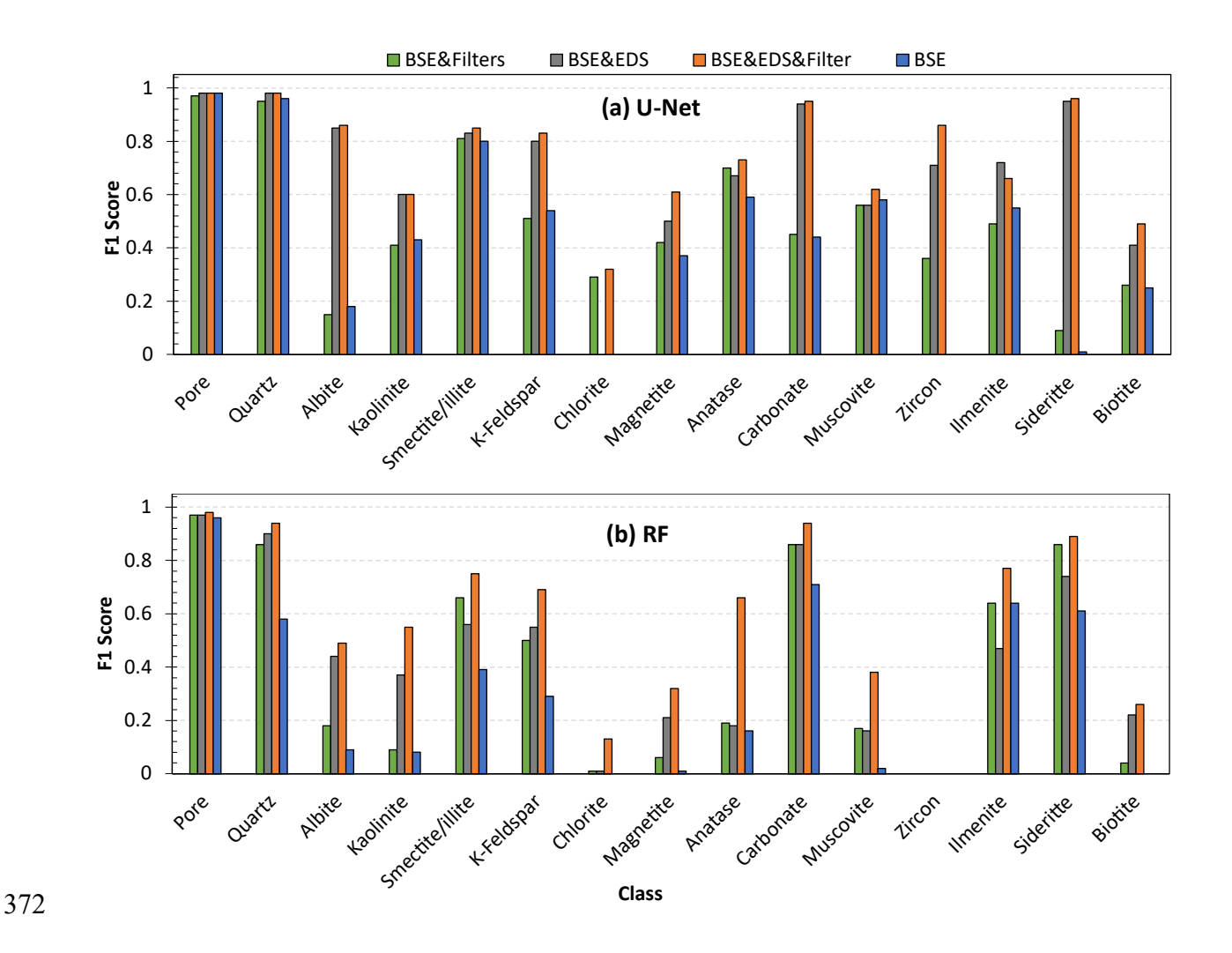


Figure 3. Performance of U-Net deep learning (a) and Random Forest machine learning (b) models for different mineral classes in pooled dataset.

When filter extracted features are considered in addition to the grayscale BSE images (green in Fig. 3), a higher performance for both models is evident. The filters extract features such as texture, size, edges, etc. which improve the predictive performance of the model, especially for minerals with similar grayscale intensity (e.g., quartz and K-feldspar). The performance of models in predicting chlorite, zircon, smectite/illite and muscovite significantly improved, particularly for the Random Forest model. The filtered-based model has a comparable performance to the BSE-EDS based model (the dark gray in Fig. 3), highlighting the significant improvement of mineral

segmentation by simply utilizing filtering techniques. This is particularly valuable in cases when EDS elemental maps are not available.

 Integrating the EDS elemental map and filtering techniques (in Fig 3) further improves the results by considering both extracted features and elemental maps along with the BSE values. The resulting accuracy improves from 56% to 92% for Random Forest and 88% to 96% for the U-Net model, which also is shown visually in Figure 4 and 5. This also has noted success in predicting phases with low volume fractions, minority classes. These phases are difficult to predict and result in low performance of the associated classes due to data scarcity. An improvement in prediction is evident in the pooled dataset using the BSE, EDS, and filter images as input. This results in prediction of minority classes such as chlorite that are not predicted by any other methods. In addition, the performance in predictions of muscovite is significantly higher than that in any other methods in both models. In summary, the pooled dataset with the BSE&EDS&Filter input variables set has the highest accuracy and F1-Score and thus was selected as the final model.

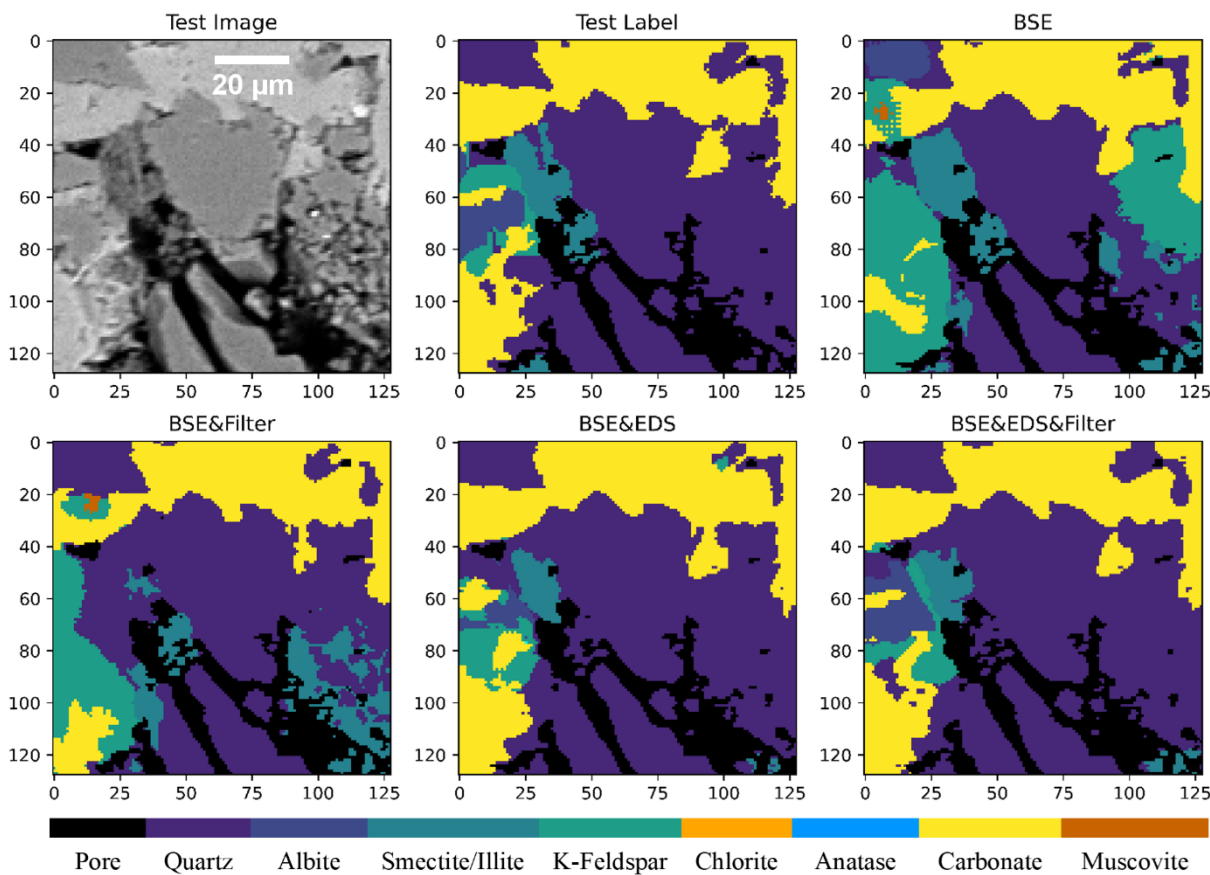


Figure 4. Visual performance of U-Net on different classes in the pooled dataset. Vertical and horizontal axes demonstrate pixel numbers with 0.71 µm resolution.

Both models show good performance for prediction of pore classes. Based on Figure 3, the "pore" class reaches a high F1-score of 96% to 98%. This highlights the capability of the models to automatically predict the sample pore pixels. Thus, obtained porosity values, which are an important characteristic of a sample and used in reactive transport simulations, are almost identical to the ground-truth data.

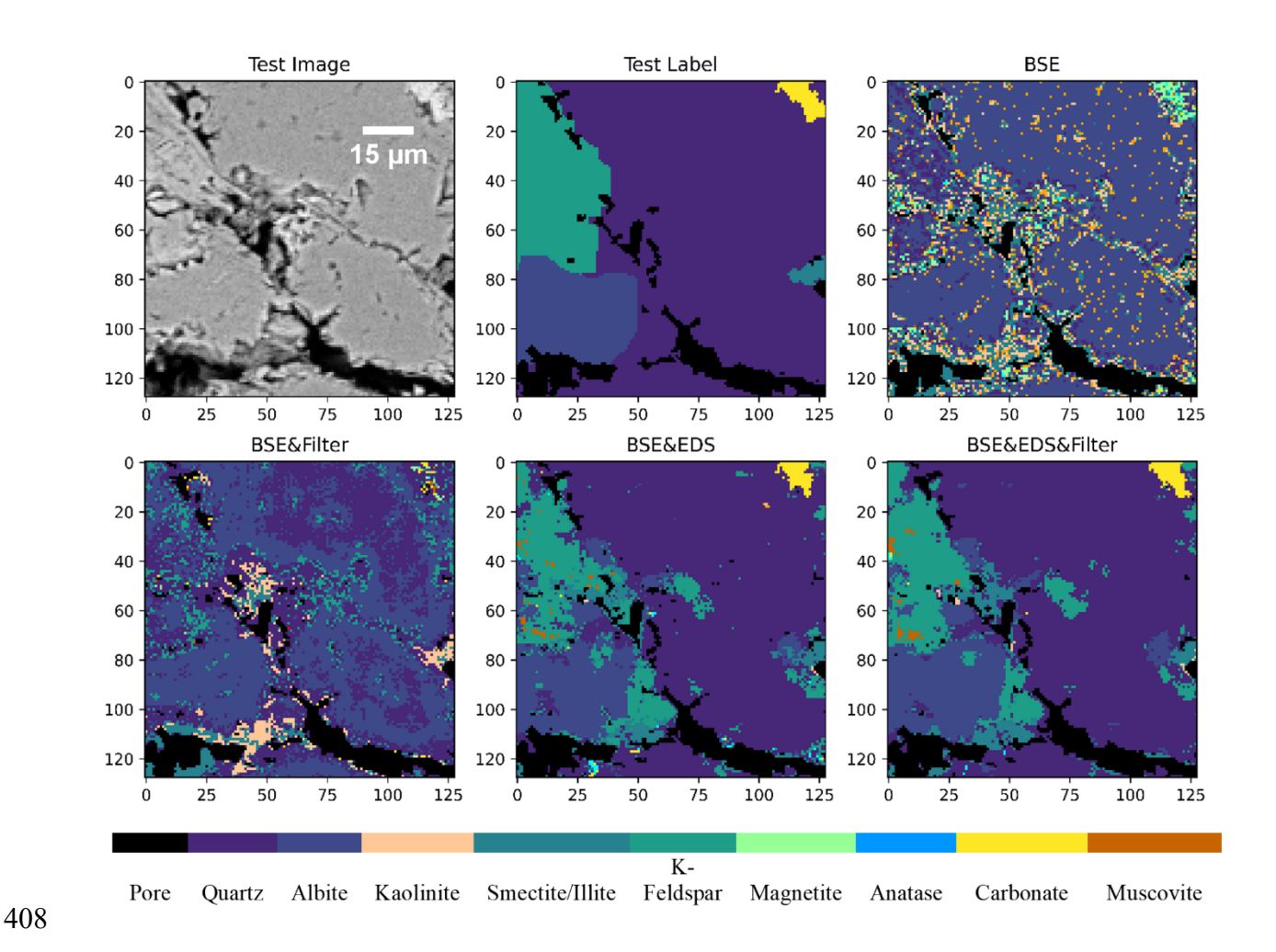


Figure 5. Visual performance of the RF model on different mineral classes in the pooled dataset.

Vertical and horizontal axes demonstrate pixel numbers with 0.71 µm resolution.

The high F1-score accuracy for most of the classes obtained from the U-Net framework (i.e., the U-Net with pooled dataset and the BSE&EDS&Filter input variable set) reveals the robustness of the framework to various ranges of grayscale inputs since it relies more on extracted features and elemental maps. These features are also important in the Random Forest model where the "mean decrease in Gini Impurity" is used here to rank the input variables for the Random Forest model to determine the most important variables for mineral/pore segmentation. Figure 6 shows the resulting relative rank where the higher numbers indicate a higher contribution to

successful classification. As shown, the median filter has the highest rank followed by the Ti elemental map. The results reveal the higher contribution of elemental images and filter extracted features compared to the BSE gray scale values.

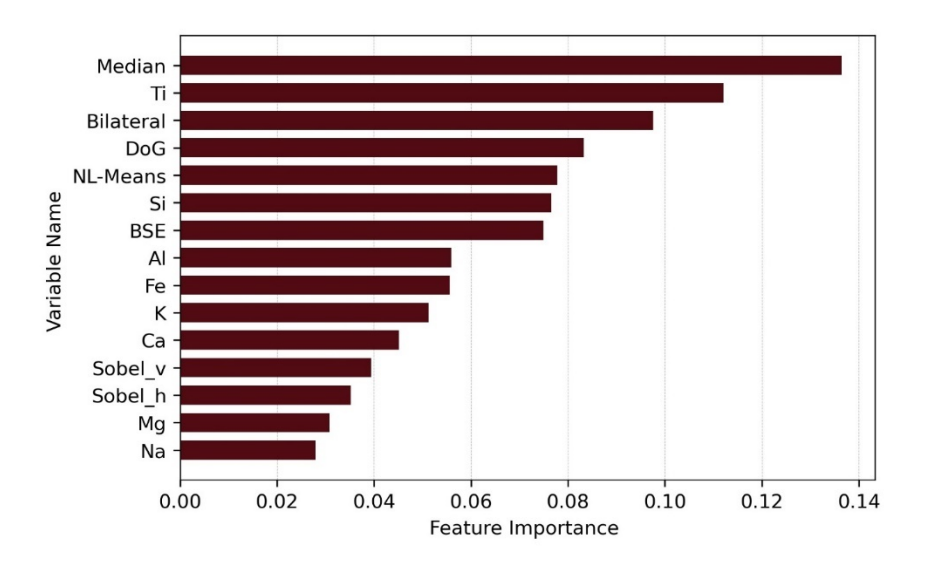


Figure 6. Rank of the input variables based on their contribution to improving segmentation (horizontal numbers are the rank of the variables called feature importance value).

3.3 Comparison of the Best Random Forest and U-Net Models

The SEM-BSE image dataset of the sandstone samples were processed and segmented for further mineral abundance and surface area analysis, using the best-trained models. Figure 7 compares the results of the best performing Random Forest and U-Net frameworks trained on the BSE&EDS&Filter input variable set of the pooled dataset. Although the pixel wise Random Forest classifier almost fails to predict some minority classes such as zircon and chlorite, it has an acceptable performance for the majority classes such as quartz (Fig. 7). On the other hand, U-Net has a higher performance, especially for muscovite minority class, and can successfully detect different classes. U-Net preserves the structural dependency of pixels and considers the neighboring pixels by utilizing the convolutional kernels which helps detect continuous features

such as edges and textures (Figure 8). Providing several extracted features helps the Random Forest model to consider this spatial dependency. Considering neighboring pixels and structural dependency when making a prediction also helps overcome the noise (based on Figure 4, 5 and 8) that inherently exists in SEM-EDS image datasets and as a result improves prediction performance.

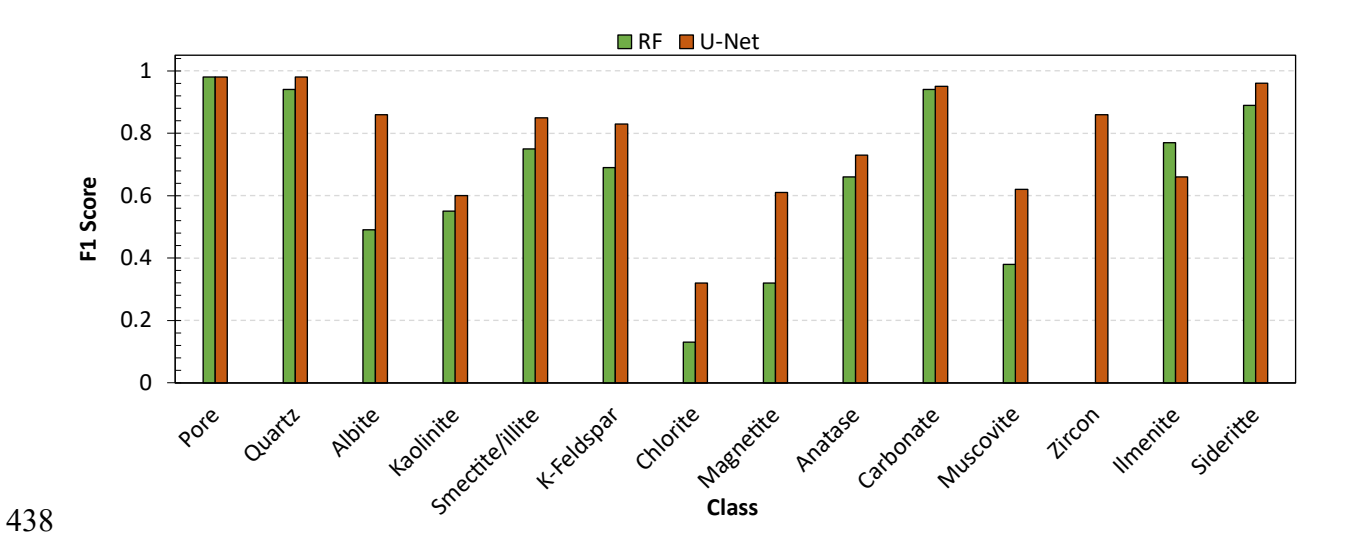


Figure 7. Comparison of the best performing U-Net and Random Forest models on predicting different mineral classes in pooled dataset.

Visualization of segmented quartz, albite, microcline, dolomite, kaolinite, illite/smectite, chlorite and pores within the samples (Fig. 4, 5 and 8 for a test subset of the samples) show that the most prevalent component of the samples is quartz, which is in agreement with XRD and ground truth data. Close inspection of these images also shows the promise machine learning has to classify variations in minerals at small scales, some of which may be missed in manual segmentation. Analysis of additional data extracted from segmented images are investigated in the next sections.

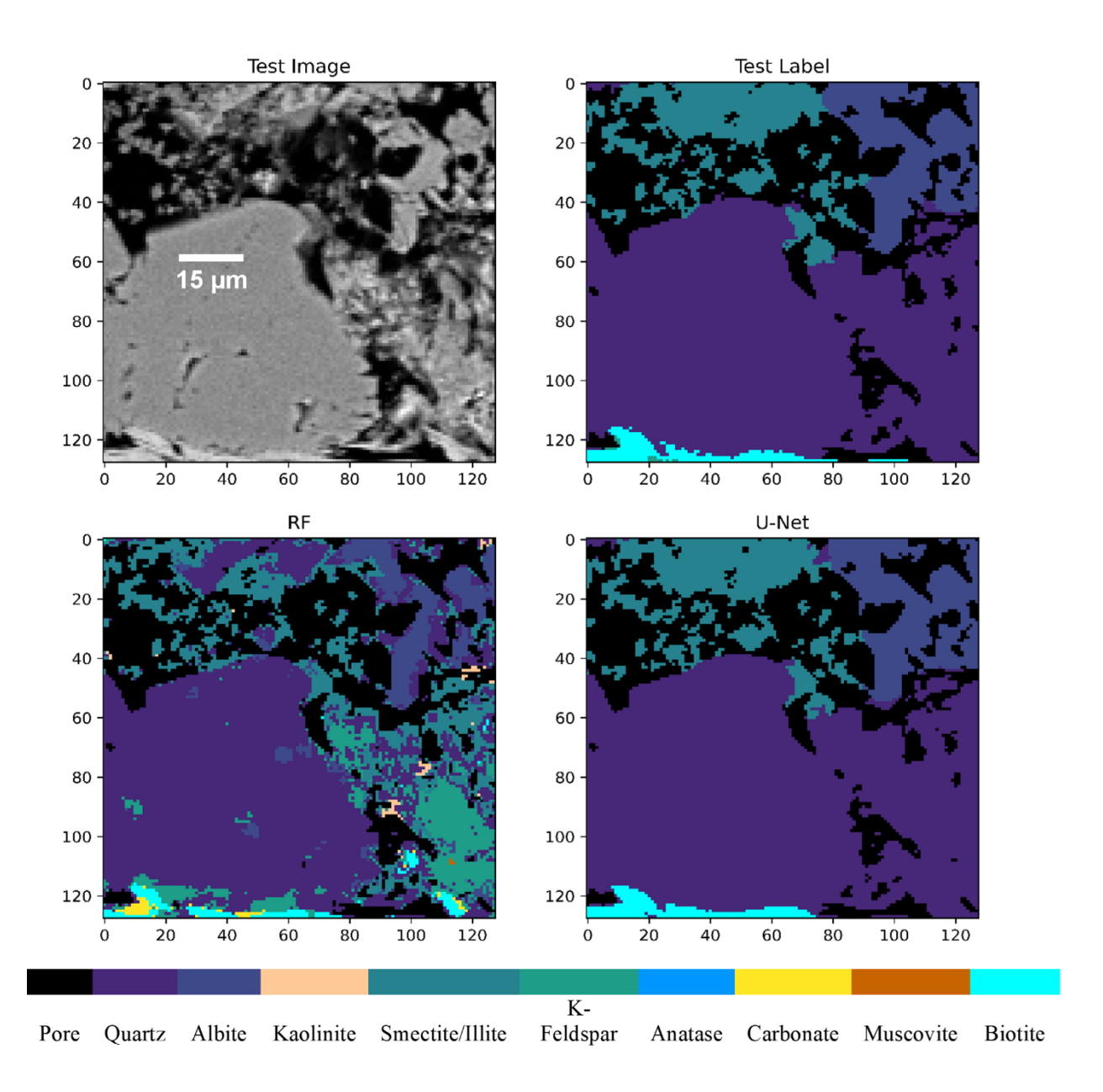


Figure 8. Visual comparison of the best performing U-Net and Random Forest models for predicting different mineral classes in pooled dataset. Vertical and horizontal axes demonstrate pixel numbers with 0.71 µm resolution.

3.4 Mineral/pore abundance and mineral accessibility analysis

453

454

455

456

457

458

459

460

461

462

463

464

465

466

467

468

469

470

471

472

473

474

475

The abundance and accessibility of minerals in segmented images for test dataset (15% of total images in pooled dataset) are given in Table 3. Results of mineral quantification indicate that overall quartz has the highest abundance among phases, followed by carbonate minerals (combined) and K-feldspar. This is also evident in the predicted results for individual datasets. Given the comparison of the results obtained from Random Forest and U-Net models with the ground truth data and considering abundance and accessibility as evaluation metrics, quartz (Abundance = 76.83% and Accessibility = 57.61%) is slightly underestimated (Abundance = 72.62% and Accessibility = 44.79%) by Random Forest and slightly overestimated by U-Net (Abundance = 77.72% and Accessibility= 55.86%). The results for other minerals, provided in Table 3, show a similar performance in which U-Net has a better result and less difference to the ground truth data compared to the Random Forest model predictions. Note that ground truth data was cross validated with XRD results and therefore U-Net model results is aligned with XRD data. In general, the observed differences in volume percentages are reasonable with most minerals within few percent agreement with the ground truth abundances. There is a larger variation evident among predicted accessibility with as much as 12% variation between predicted accessibility and the ground truth value with the largest difference for smectite/illite.

These results show the capability of machine learning models, especially U-Net, in characterizing geological samples to assess mineralogy and reactivity. A larger, balanced dataset with various mineral distributions could enhance model training and thus improve the results even further.

Table 3. Predicted abundance and accessibility values obtained from the models and the corresponding ground truth data.

Mineral	Rank	Chemical formula	Method	Abundance (%)	Accessibility (%)

		<u> </u>	ground truth	76.83	57.61
Quartz	1	${ m SiO}_2$	RF	72.62	44.79
		5102	U-Net	77.72	55.86
Albite	11		ground truth	2.02	2.66
		NaAlSi 3O 8	RF	4.22	3.49
			U-Net	2.40	3.97
			ground truth	0.39	4.85
Kaolinite	5	$Al_2Si_2O_5(OH)_4$	RF	0.64	7.18
			U-Net	0.27	3.25
		TiO ₂	ground truth	0.04	0.05
Anatase	3		RF	0.03	0.03
			U-Net	0.03	0.05
			ground truth	8.47	3.45
Carbonate	14	CaCO ₃ /MgCO ₃ ·CaCO ₃	RF	8.35	2.96
			U-Net	6.76	2.46
			ground truth	0.05	0.01
Biotite	8	$K(Mg,Fe++)_3[AlSi_3O_{10}(OH,F)_2$	RF	0.18	0.04
			U-Net	0.11	0.12
		KAl ₂ [AlSi ₃ O ₁₀]	ground truth	0.81	1.49
Muscovite	6		RF	0.37	0.58
			U-Net	0.42	1.00
		KAlSi ₃ O ₈	ground truth	3.86	3.30
K-feldspar	10		RF	4.12	2.07
			U-Net	4.82	3.98
	13	Fe(Ca,Mg)(CO ₃) ₂	ground truth	0.96	0.30
Siderite			RF	0.88	0.22
			U-Net	1.22	0.39
	9	K 0.65 Al 2 [Al 0.65 Si 3.35	ground truth	6.45	25.79
Smectite/Illite			RF	8.18	37.90
		O ₁₀](OH) ₂	U-Net	5.99	28.08
	12		ground truth	0.09	0.32
Magnetite		Fe ₃ O ₄	RF	0.36	0.39
			U-Net	0.20	0.57
	2	ZrSiO ₄	ground truth	0.00	0.00
Zircon			RF	0.00	0.00
			U-Net	0.03	0.00
Ilmenite	4	(Fe,Ti) ₂ O ₃	ground truth	0.03	0.08
			RF	0.03	0.06
		\ \ \ \ \ \ \ \ \ \ \ \ \ \ \ \ \ \ \	U-Net	0.02	0.04
			ground truth	0.01	0.10
Chlorite	7	ClO ⁻ ₂	RF	0.02	0.30
	<u> </u>		U-Net	0.02	0.24

3.4.1 Mineral dissolution risk assessment map for potential reactive surface area evolution

This section compares and contrasts the obtained dissolution rank from the U-Net mineral/pore results with ground truth data. Figure 9 shows the potential dissolution rank for U-Net predicted K-feldspar mineral pixels obtained based on the maximum dissolution rank of neighboring pixels to the pixels of interest. As evident in the figure, variations in the dissolution risk ranking can be observed. Regions that are most available for reaction have the highest scores and are shown in blue. These surfaces are adjacent to pore space. Variations in the anticipated availability of other surfaces for reaction are indicated by varying color/risk number. Higher numbers are anticipated to be accessible for reaction more quickly than those with lower numbers.

The overall trend in the predicted image is similar to the ground truth image. This reveals the reliability of the U-Net model not only for predicting the mineralogy, and as a result, reactivity, of each pixel but also the ability of the trained framework to correctly predict neighboring pixels that may impact the potential reactivity of the pixels of interest. The results obtained based on this image show the U-Net predicted pore/mineral segmented map can be utilized to inform the reactive transport models over time scale.

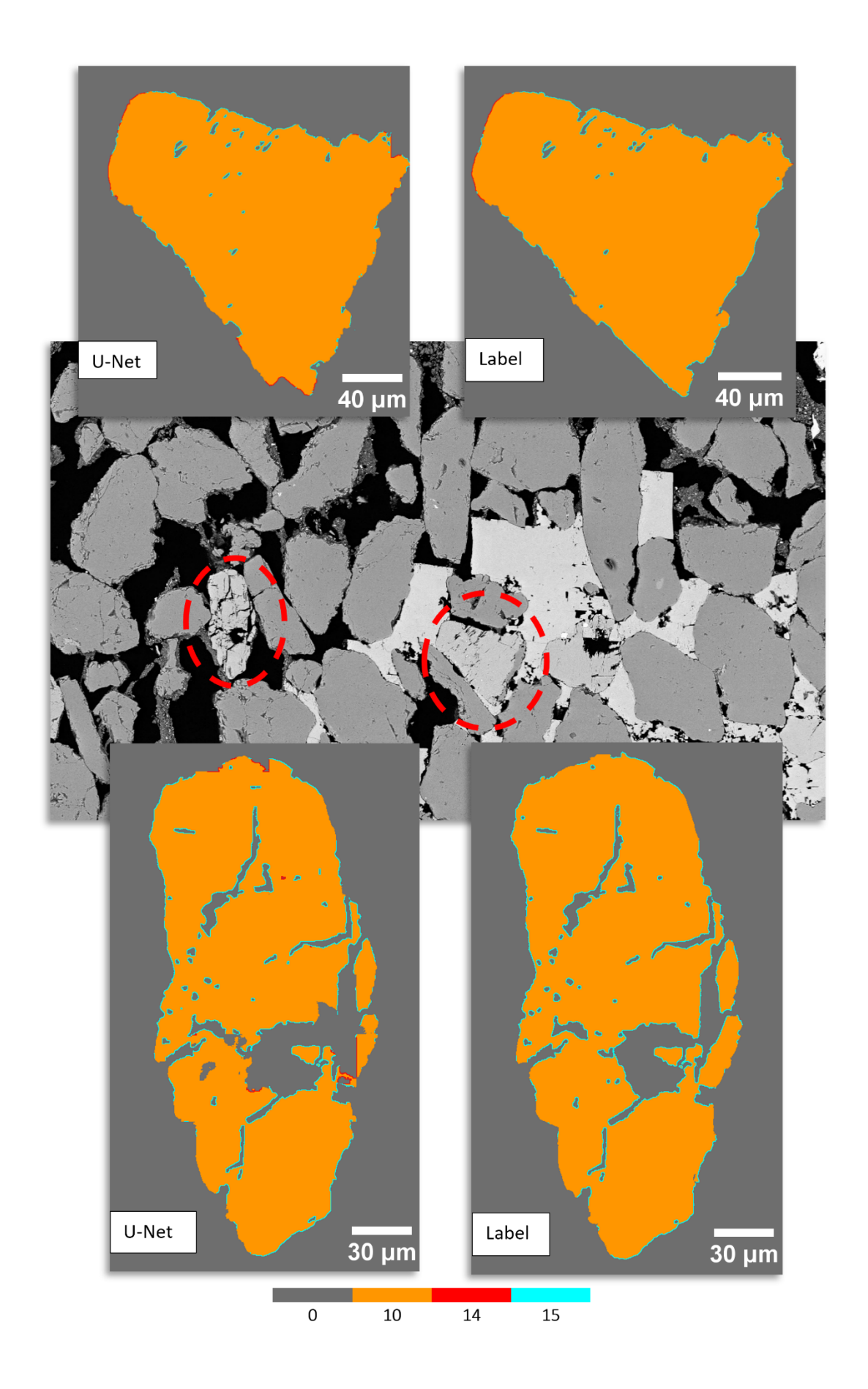


Figure 9. Ranked mineral dissolution risk assessment map for K-feldspar (rank 10) that is adjacent to rank 15 (pores) and 14 (carbonate), with 0.34 µm resolution. Rank zero shows pixels that are not on the surface of the mineral of interest.

4. Conclusions

This study evaluated the performance of Random Forest and U-Net models for mineral/pore phase segmentation and surface analysis of SEM images of various sandstone samples. This is achieved by providing a framework that not only evaluates the results on each pixel but also takes the predicted neighboring pixels into account. The performance of the models was investigated on a series of individual datasets as well as a combined dataset that included data from various samples, each with different grayscale intensity variation, in addition to EDS maps and filter data. It was shown that the performance of both platforms reaches the highest score when all BSE, EDS, filter data are used as input variables on the pooled dataset to train the models. Using those inputs, the U-Net model achieved the highest performance accuracy of 96%.

In general, the results from the U-Net model had a higher performance compared to the Random Forest model in predicting each class and thus a more reliable phase segmentation in different samples. In addition, the U-Net model had a better performance for surface quantification and had comparable results to the ground truth data for mineral abundances and accessibility. By comparing the results of the individual dataset to the pooled one, it can be concluded that using larger datasets (i.e., pooled dataset) can improve the results even further which is an inherent characteristic of machine learning models.

The results obtained from comparing the models with different input variable sets showed the trained models relied more on extracted features and information obtained from EDS elemental

maps. Feature importance ranking in the Random Forest model confirmed this conclusion. It also showed the median and gaussian filters had the highest contribution in phase segmentation due to removing unwanted noise and providing more integrated phases. Relying on extracted features provided a more robust solution to grayscale variation from one dataset to another since the grayscale intensity may vary but extracted features are more or less similar in different datasets.

Finally, the mineral risk assessment map was proposed. This provided a robust solution to identify the locations susceptible for dissolution and is recommended to be used in conjunction with the machine learning platforms. This map can capture variations in surface reactivity due to differences in accessibility where some surfaces are in contact with pores and thus accessible for reaction while others are occluded by mineral coatings. Occluded surfaces will be accessible for reaction once the coating phase dissolves. This may be a promising approach to considering the potential evolution of reactive surfaces.

The intelligent segmentation and surface analysis framework in this work is promising for accelerating the processing of SEM data as well as reducing the need for post-process filtration. The obtained parameters can be utilized to enhance understanding of sample characteristics including mineralogy as well as reactive properties. Data such as porosity and mineral volume fractions can be quantified from processed maps and used to inform reactive transport simulations.

Acknowledgement

This material is based upon work supported by the National Science Foundation under Grant

535 No: 1847243

536 Supplementary and codes

- The labeling and Normalizing&Cropping, Filtering, Accessibility&Abundance Total, and ranked
- 538 mineral dissolution risk assessment map codes and images can be found at
- 539 https://github.com/Parisa-Asadi/Machine-learning-for-Surface-Areas-Analysis.

References

- Asadi, P., & Beckingham, L. E. (2021). Integrating Machine/Deep Learning Methods and Filtering
- Techniques for Reliable Mineral Phase Segmentation of 3D X-ray Computed Tomography
- 543 Images. *Energies*, 14(15), 4595.
- Asadi, P., & Tian, D. (2021). Estimating leaf wetness duration with machine learning and climate
- reanalysis data. *Agricultural and Forest Meteorology*, 307, 108548.
- Anovitz, L. M., Beckingham, L. E., Sheets, J. M., & Cole, D. R. (2022). A Quantitative Approach
- 547 to the Analysis of Reactive Mineralogy and Surface Area. ACS Earth and Space Chemistry, 6(2),
- 548 272-287.
- Brantley, S. L. (2008). Kinetics of mineral dissolution. In *Kinetics of water-rock interaction* (pp.
- 550 151-210). Springer, NY, USA.
- 551 Bradski, L. (2001). Random forests. Machine learning, 45(1), 5-32.
- Bradski, G., & Kaehler, A. (2008). Learning OpenCV: Computer vision with the OpenCV library.
- 553 O'Reilly Media, Inc. Ca, USA.
- Beckingham, L.E., Steefel, C.I., Swift, A.M., Voltolini, M., Yang, L., Anovitz, L.M., Sheets, J.M.,
- Cole, D.R., Kneafsey, T.J., Mitnick, E.H. and Zhang, S. (2017). Evaluation of accessible mineral

- surface areas for improved prediction of mineral reaction rates in porous media. Geochimica et
- 557 *Cosmochimica Acta*, 205, 31-49.
- Brunhoeber, O. M., Anovitz, L. M., Asadi, P., & Beckingham, L. E. (2021). Role of mineralogy
- in controlling fracture formation. ACS Earth and Space Chemistry, 5(11), 3104-3114.
- 560 Chen, X. Y., Teng, F. Z., Huang, K. J., & Algeo, T. J. (2020a). Intensified chemical weathering
- during Early Triassic revealed by magnesium isotopes. Geochimica et Cosmochimica Acta, 287,
- 562 263-276.
- 563 Chen, Z., Liu, X., Yang, J., Little, E., & Zhou, Y. (2020b). Deep learning-based method for SEM
- image segmentation in mineral characterization, an example from Duvernay Shale samples in
- Western Canada Sedimentary Basin. Computers & Geosciences, 138, 104450.
- Deng, H., Fitts, J. P., Tappero, R. V., Kim, J. J., & Peters, C. A. (2020). Acid erosion of carbonate
- 567 fractures and accessibility of arsenic-bearing minerals: In Operando synchrotron-based
- 568 microfluidic experiment. Environmental Science & Technology, 54(19), 12502-12510.
- 569 Esene, C., Zendehboudi, S., Aborig, A., & Shiri, H. (2019). A modeling strategy to investigate
- 570 carbonated water injection for EOR and CO2 sequestration. Fuel, 252, 710-721.
- Guan, S. (2012). Modeling geomechanical property changes using well logging and pressure data
- in a carbon dioxide enhanced oil recovery reservoir. *ProQuest LLC*. Co, USA.
- 573 Iloejesi, C. O., & Beckingham, L. E. (2021a). Assessment of geochemical limitations to utilizing
- 574 CO2 as a cushion gas in compressed energy storage systems. Environmental engineering
- 575 science, 38(3), 115-126.

- 576 Iloejesi, C. O., & Beckingham, L. E. (2021b). Influence of storage period on the geochemical
- evolution of a compressed energy storage system. Frontiers in Water, 3, 100-113.
- Koohi-Fayegh, S., & Rosen, M. A. (2020). A review of energy storage types, applications and
- recent developments. *Journal of Energy Storage*, 27, 101047.
- Kim, J. J., Ling, F. T., Plattenberger, D. A., Clarens, A. F., Lanzirotti, A., Newville, M., & Peters,
- 581 C. A. (2021). SMART mineral mapping: Synchrotron-based machine learning approach for 2D
- 582 characterization with coupled micro XRF-XRD. Computers & Geosciences, 156, 104898.
- 583 Karimpouli, S., & Tahmasebi, P. (2019). Segmentation of digital rock images using deep
- 584 convolutional autoencoder networks. Computers & geosciences, 126, 142-150.
- 585 Li, C., Wang, D., & Kong, L. (2021). Application of machine learning techniques in mineral
- classification for scanning electron microscopy-energy dispersive X-ray spectroscopy (SEM-EDS)
- 587 images. Journal of Petroleum Science and Engineering, 200, 108178.
- Luhmann, A. J., Tutolo, B. M., Bagley, B. C., Mildner, D. F., Seyfried Jr, W. E., & Saar, M. O.
- 589 (2017). Permeability, porosity, and mineral surface area changes in basalt cores induced by
- reactive transport of CO2-rich brine. Water Resources Research, 53(3), 1908-1927.
- Landrot, G., Ajo-Franklin, J. B., Yang, L., Cabrini, S., & Steefel, C. I. (2012). Measurement of
- accessible reactive surface area in a sandstone, with application to CO2 mineralization. *Chemical*
- 593 *Geology*, 318, 113-125.
- Ma, J., Ahkami, M., Saar, M. O., & Kong, X. Z. (2021). Quantification of mineral accessible
- surface area and flow-dependent fluid-mineral reactivity at the pore scale. *Chemical Geology*, 563,
- 596 120042.

- Mahdikhani, M., Bamshad, O., & Shirvani, M. F. (2018). Mechanical properties and durability of
- 598 concrete specimens containing nano silica in sulfuric acid rain condition. Construction and
- 599 Building Materials, 167, 929-935.
- Mohammadian, E., Kheirollahi, M., Liu, B., Ostadhassan, M., & Sabet, M. (2022). A case study
- of petrophysical rock typing and permeability prediction using machine learning in a heterogenous
- 602 carbonate reservoir in Iran. Scientific Reports, 12(1), 1-15.
- Pirrie, D., Butcher, A. R., Power, M. R., Gottlieb, P., & Miller, G. L. (2004). Rapid quantitative
- mineral and phase analysis using automated scanning electron microscopy (QemSCAN); potential
- applications in forensic geoscience. Geological Society, London, UK. Special Publications, 232(1),
- 606 123-136.
- Pedregosa, F., Varoquaux, G., Gramfort, A., Michel, V., Thirion, B., Grisel, O., Blondel, M.,
- Prettenhofer, P., Weiss, R., Dubourg, V. & Vanderplas, J. (2011). Scikit-learn: Machine learning
- in Python. *The Journal of Machine Learning Research*, 12, 2825-2830.
- Peters, C. A. (2009). Accessibilities of reactive minerals in consolidated sedimentary rock: An
- 611 imaging study of three sandstones. Chemical Geology, 265(1-2), 198-208.
- 612 Qin, F., & Beckingham, L. E. (2019). Impact of image resolution on quantification of mineral
- abundances and accessible surface areas. *Chemical Geology*, *523*, 31-41.
- Ronneberger, O., Fischer, P., & Brox, T. (2015, October). U-net: Convolutional networks for
- 615 biomedical image segmentation. In International Conference on Medical Image Computing and
- 616 Computer-assisted Intervention (pp. 234-241). Springer, Cham. London, UK.

- 617 Salek, Md. F., Qin, F., Asadi, P., Iloejesi, C., Brunhoeber, O., Mahmood, M., Beckingham,
- 618 L.E. (2022). Impact of pore connectivity on quantification of mineral accessibility in sandstone
- 619 samples. ACS Earth Space Chemistry . Submitted.
- 620 Soong, Y., Howard, B.H., Dilmore, R.M., Haljasmaa, I., Crandall, D.M., Zhang, L., Zhang, W.,
- 621 Lin, R., Irdi, G.A., Romanov, V.N. and Mclendon, T.R. (2016). CO2/brine/rock interactions in
- 622 Lower Tuscaloosa formation. *Greenhouse Gases: Science and Technology*, 6(6), 824–837.
- 623 Seyyedi, M., Sohrabi, M., Sisson, A., & Ireland, S. (2018). Quantification of oil recovery
- efficiency, CO2 storage potential, and fluid-rock interactions by CWI in heterogeneous sandstone
- oil reservoirs. *Journal of Molecular Liquids*, 249, 779-788.
- 626 Suthaharan, S. (2016). Machine learning models and algorithms for big data classification. *Integr.*
- 627 Ser. Inf. Syst, 36, 1-12.
- Van der Walt, S., Schönberger, J.L., Nunez-Iglesias, J., Boulogne, F., Warner, J.D., Yager, N.,
- 629 Gouillart, E. & Yu, T. (2014). scikit-image: image processing in Python. *PeerJ*, 2, e453.
- Yadav, S. K., & Chakrapani, G. J. (2006). Dissolution kinetics of rock-water interactions and its
- 631 implications. Current Science, 932-937.
- Yoon, H., Melander, D., & Verzi, S. J. (2021, March). Machine learning application for
- 633 permeability estimation of three-dimensional rock images. In *The AAAI 2021 Spring Symposium*
- on Combining Artificial Intelligence and Machine Learning with Physical Sciences (AAAI-MLPS
- 635 2021), Stanford, CA, USA, http://ceur-ws.org/Vol-2964/article 191.pdf.

Zhang, Y., Chen, J., & Li, Y. (2022). Segmentation and quantitative analysis of geological fracture:
a deep transfer learning approach based on borehole televiewer image. *Arabian Journal of Geosciences*, 15(3), 1-17.
Zhang, S., Yang, L., DePaolo, D. J., & Steefel, C. I. (2015). Chemical affinity and pH effects on chlorite dissolution kinetics under geological CO2 sequestration related conditions. *Chemical Geology*, 396, 208-217.